Structural and Multidisciplinary Optimization (2025) 68:179
https://doi.org/10.1007/s00158-025-04120-w

RESEARCH PAPER

Risk-based design optimization for powder bed fusion metal additive manufacturing

Yulin Guo[1] · Boris Kramer[1]

Received: 13 May 2025 / Revised: 23 July 2025 / Accepted: 12 August 2025

Abstract

Powder bed fusion is a widely used additive manufacturing (AM) process for producing complex, small-batch parts that are impractical to manufacture using conventional methods. However, its broader adoption is hindered by process-induced defects. The challenge in AM stems from inherent material and process uncertainties. Therefore, it is critical to account for these uncertainties in the design optimization and control of powder bed fusion AM processes. In this work, we formulate and solve a design optimization under uncertainty problem for a powder bed fusion metal AM process. Our objective is to minimize energy consumption while enforcing a risk-based constraint formulated with a buffered probability of failure on residual stress, along with a constraint on melting temperature to ensure a successful build. We use surrogate models for the residual stress and temperature snapshots to accelerate optimization; we train these models using data from high-fidelity finite element simulations. We validate the optimization results through additional high-fidelity simulations. The validated results demonstrate that the proposed optimization reduces energy consumption, enhances process reliability, and contributes to more robust and sustainable additive manufacturing.

Keywords Risk · Design optimization · Powder bed fusion · Additive manufacturing · Titanium · Buffered probability of failure · Conditional value-at-risk · Superquantile · Singular value decomposition · Active subspace · Surrogate modeling

1 Introduction

Additive manufacturing (AM) is the process of joining materials to make parts from 3D model data, usually layer upon layer, as opposed to subtractive manufacturing and formative manufacturing methodologies (International Organization for Standardization, American Society for Testing and Materials 2021; Gibson et al. 2021). It has grown in popularity due to its speed, low labor cost, customization ability, and ability to make highly complex geometric designs compared to traditional manufacturing methodologies, such as milling and injection molding. A variety of materials, including polymers, metals, and ceramics, are available to provide the unique attributes needed to satisfy the engineering requirements of AM parts in aerospace, automotive, medical devices, and other industries (Shapiro et al. 2016; Vasco 2021; Seoane-Viaño et al. 2021; Murr 2018; Wang et al. 2024). The American Society for Testing and Materials classifies AM processes into seven categories: binder jetting, directed energy deposition, material extrusion, material jetting, powder bed fusion, sheet lamination, and vat photopolymerization (International Organization for Standardization, American Society for Testing and Materials 2021). Several additive manufacturing processes are available for metallic materials, with each process utilizing specific material forms: metal sheets for sheet lamination, metal rods or wires for material extrusion, metal wires for directed energy deposition, and metal powders for binder jetting and powder bed fusion (Konda Gokuldoss et al. 2017). Powder bed fusion methods have been applied to a wide range of metallic materials, such as Fe-based alloys (Wu et al. 2014), Ni-based alloys (Lu et al. 2015), Ti-based alloys (Gong et al. 2015), Co-based alloys (Wei et al. 2018), and Cu-based alloys (Lu et al. 2021). Within the powder bed fusion methods, electron beam melting and selective laser melting (also known as laser beam melting) are two common methods to produce metallic parts where the powder is melted and fused by an

Responsible Editor: Zhen Hu.

✉ Boris Kramer
bmkramer@ucsd.edu

[1] Department of Mechanical and Aerospace Engineering, University of California SanDiego, La Jolla, CA, USA

electron or laser beam. These two processes share the same fundamental workflow with differences in their operating environments. In electron beam melting, a heated powder bed and a vacuum chamber are used. The vacuum guides and focuses the electron beam. By comparison, selective laser melting operates with a cold powder bed inside a closed chamber filled with inert gases, such as N_2 or Ar, which prevents oxidation of the metal powder during melting (Fu and Guo 2014; Konda Gokuldoss et al. 2017).

The selective laser melting process involves over 50 parameters, including laser power, scanning speed, hatch distance, and overlaps; the electron beam melting process encompasses even more parameters, such as beam focus, beam diameter, beam line spacing, plate temperature, preheating temperature, contour strategy, and scan strategy (Spears and Gold 2016; Konda Gokuldoss et al. 2017). Improper selection of process parameters can lead to defects such as high surface roughness, pores and voids, cracks, delaminations, or distortions, which significantly compromises part quality (Gong et al. 2015; Yan et al. 2017; Bartlett and Li 2019; Galarraga et al. 2016). For example, higher scanning speeds increase the length-to-diameter ratio of the molten pool present in the manufacturing process. When this ratio exceeds π, it causes the balling effect (breaking up of the molten pool into spherical particles). This phenomenon degrades the surface integrity of the final components. Scanning speed and cooling rate can also affect the grain size, which in turn affects the mechanical properties (Corbin et al. 2018; Yadroitsev et al. 2013).

The relationships between process parameters and part quality involve complex nonlinear correlations that do not allow for explicit mathematical formulation (Cao et al. 2021). Despite the growing adoption of AM technologies, the field lacks comprehensive guidelines for selecting appropriate AM processes based on material requirements and desired part properties (Konda Gokuldoss et al. 2017). Process parameter optimization for AM processes has been extensively studied using design of experiments (DoE) methods, including factorial design (Gong et al. 2014; Oyesola et al. 2021), central composite design (Bhardwaj et al. 2019; Elsayed et al. 2018), and Taguchi methods (Sun et al. 2013; Gong et al. 2014). These approaches are often complemented by statistical analysis techniques, such as regression analysis (Gong et al. 2014, 2015; Shi et al. 2017) and analysis of variance (ANOVA) (Sun et al. 2013; Elsayed et al. 2018). These optimization methods are time-consuming because they typically require evaluating multiple parameter combinations. The computational burden grows exponentially as each additional parameter requires testing across multiple intervals, either through numerical simulations or physical experiments. To address these limitations, AM process parameter optimization using surrogate models has been proposed in literature, with studies incorporating Gaussian process modeling (Meng and Zhang 2020; Cao et al. 2021) and various machine learning approaches (Gaikwad et al. 2020).

The uncertainties in AM process parameters propagate through the manufacturing process, making quantities of interest, such as the residual stress of the printed part, uncertain as well. Consequently, design for AM processes should consider uncertainties not only in the process parameters but also in the quantities related to manufactured part qualities, such as residual stress. In order to incorporate uncertainties, robust design optimization (Lee and Rahman 2021) and reliability-based design optimization (Zou and Mahadevan 2006) have been used. The former aims to minimize the sensitivity of the system performance and typically uses mean and variance as optimization objectives. It does not explicitly account for failure probability, which may result in designs that are consistent but still have unacceptable failure rates in extreme conditions. A robust design optimization approach has been proposed for process parameters in metallic additive manufacturing (Wang et al. 2019). Their work addresses uncertainties in material properties and power absorption coefficients. Reliability-based design optimization manages uncertainty by enforcing the probability of failure below specified thresholds while optimizing performance objectives. It uses a first- or second-order reliability method or Monte Carlo simulation to evaluate failure. A major limitation is the high computational cost, especially for estimating rare-event probabilities. A traditional approach is to add safety margins to the results of deterministic design optimization to compensate for uncertainties. However, this approach is inefficient, as it neither incorporates uncertainties directly into the design optimization process nor optimizes the safety margins themselves, which can potentially limit performance. Heuristic optimization methods have also been used in recent studies, such as whale optimization algorithm in Cao et al. (2021). A principled way to account for the failure magnitude integrates superquantile (also known as conditional value-at-risk, CVaR) (Rockafellar and Uryasev 2002) and buffered probability of failure (BPOF) (Rockafellar and Royset 2010) into design optimization processes. These alternative risk measures can be used either as objectives or constraints in optimization formulations (Chaudhuri et al. 2022) and eliminate the guesswork associated with choosing safety margins.

In this paper, we present a novel approach to risk-based design optimization under uncertainty for powder bed fusion metal additive manufacturing (AM), advancing robust and sustainable process design. Our contributions are both towards the problem formulation, as well as its solution. First, in the optimization formulation, we incorporate a buffered probability of failure (BPOF) constraint, which penalizes both the frequency and severity of process failures. This enables simultaneous improvement in energy efficiency and process reliability. Second, for the solution, we develop accurate and efficient surrogate models that leverage high-fidelity thermal-mechanical simulation data to map complex temperature histories and residual stress fields into low-dimensional spaces. This facilitates rapid optimization of process parameters. Third, we validate the surrogate-based optimization results through additional high-fidelity simulations. These validation results confirm that the optimizer reduces energy without compromising the part quality, demonstrating that our proposed approach advances robust and sustainable metal additive manufacturing.

The rest of this paper is organized as follows. In Sect. 2, we present an overview of risk-based design optimization. In Sect. 3, we introduce the powder bed fusion process, its thermal and mechanical governing equations, finite element modeling, residual stress development in manufactured parts, and mitigation strategies. In Sect. 4, we then present the design under uncertainty problem in full detail and cover risk-based measures, surrogate model development, and our optimization methodology. In Sect. 5, we present and analyze numerical results. Finally, we summarize our conclusions and suggest directions for future research in Sect. 6.

2 Formulation of risk-based design optimization for the powder bed fusion metal additive manufacturing problem

In powder bed fusion, the beam power and scanning speed have emerged as predominant optimization parameters across recent studies (Meng and Zhang 2020; Shi et al. 2017; Cao et al. 2021). We formulate an optimization problem with the goal to minimize the total energy consumed, which is a function of the beam power and scanning speed, subject to a threshold on the BPOF on the maximum residual stress, as well as a threshold on the maximum temperature, in a part manufactured by an electron beam melting process.

The manufacturing process is parameterized by two design variables, four random variables and six parameters. The two design variables are the scanning speed $v \in [v_L, v_U]$ and beam power $P \in [P_L, P_U]$, which form the design vector $\mathbf{d} = [v, P]^\top$. The four random variables are the preheating temperature T_0 of the machine, the yield strength Y, elastic modulus E, and bulk density ρ of the material. These variables are assumed to be statistically independent and are collected in the random vector $Z = [T_0, Y, E, \rho]^\top$. The specific heat $C_p(T)$ and thermal conductivity $\kappa(T)$ are functions of temperatures and are parameterized by coefficients, a_i and b_i, $i = 1, 2, 3$, respectively, as discussed in detail in Sects. 3.3 and 5.1. The six coefficients are taken to be deterministic parameters and are collected in a vector $\boldsymbol{\theta} = [a_1, a_2, a_3, b_1, b_2, b_3]^\top$, which we do not optimize over. We formulate the optimization problem as follows:

$$\begin{aligned} \min_{\substack{P_L \le P \le P_U,\\ v_L \le v \le v_U}} \quad & P \cdot \frac{l}{v} \\ \text{subject to} \quad & \bar{p}(\sigma_{\max}(\mathbf{d}, Z;\boldsymbol{\theta})) \le 1-\alpha_T,\\ & T_{\text{liq}} < T_{\max}(\mathbf{d}, Z;\boldsymbol{\theta}) < 1.1 \times T_{\text{liq}}, \end{aligned} \tag{1}$$

where l is the length length of the part (the laser's total scanning distance), l/v is the total time that the beam is applied, is the BPOF, is the desired reliability level, is the maximum residual stress, is the maximum temperature in the temperature history, and is the liquidus temperature of the material, see Sect. 5.1 for more details and specific values.Next, we discuss the powder bed fusion application, including its governing equations to determine $\sigma_{\max}$ and $T_{\max}$. Then, in Sect. 4, we discuss the reliability constraint on $\sigma_{\max}$ followed by the solution to the optimization problem (1).

3 Powder bed fusion application

We introduce the electron beam melting process in Sect. 3.1 and the residual stress that arises in additively manufactured parts in Sect. 3.2. We then discuss the thermal and mechanical models governing the powder bed fusion process in Sects. 3.3 and 3.4. Finally, we present the finite element models used to simulate the manufacturing process in Sect. 3.5.

3.1 Electron beam melting process

In an electron beam melting powder bed fusion process, a thin layer of powder is deposited over a substrate plate or previously deposited layers, and then an electron beam selectively melts and fuses the powder particles according to the desired part model data. This layer-by-layer process continues until the complete part is built. When the electron beam scans across the powder surface, energy transfers from the top surface to the subsurface. The powder melts when the temperature reaches the material's liquidus temperature. Figure 1 shows the schematic of the electron beam melting machine and a part being built, including the molten pool, solidification zone, substrate, and unmelted powder.

3.2 Residual stress and treatment

In the electron beam melting process, rapid heating of the upper surface combined with slow heat conduction of the underlying layers creates a steep temperature gradient. This gradient generates convection currents that affect material flow, creates surface tension variations in the molten pool, and induces high internal stresses. Expansion

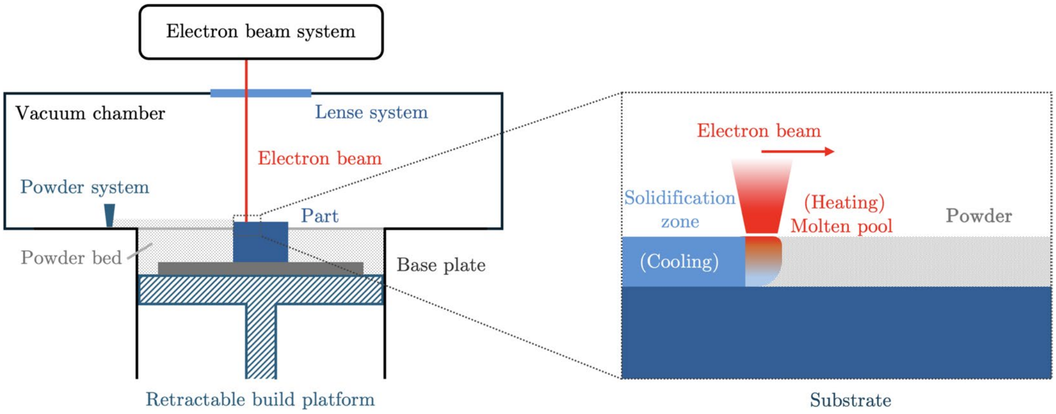

Fig. 1 Schematic of an electron beam melting machine and the printing process

of the heated layer is restricted by the vicinity area, resulting in compressive stress at the surface. Cooling takes place as the heat source moves away, and the contraction of the top layer is then restricted by the surrounding area. This results in tensile residual stress on the top surface. These tensile residual stresses accumulate across multiple scan paths, potentially leading to delamination or crack formation. In addition, the differential cooling and shrinkage between layers causes the top layers to become shorter than the bottom layers. This dimensional mismatch creates a bending moment that distorts the part upward toward the beam direction (Fu and Guo 2014; Li et al. 2018).

To mitigate residual stress, in situ control and post-process control methods have been studied. In situ controls for additive manufacturing includes both mechanical and thermal methods. Mechanical approaches, such as laser shock peening and rolling, generate compressive pressure to counterbalance residual stresses. However, laser shock peening, while effective, significantly extends printing time and poses integration challenges with powder bed fusion systems (Kalentics et al. 2017). Thermal gradient control methods reduce residual stress by homogenizing temperature distribution throughout the process. However, they can cause larger grain sizes and anisotropic microstructure, require precise temperature calibration based on alloy properties, and consume more energy (Everton et al. 2016; Chia et al. 2022). Post-heat treatment processes are widely utilized to restore homogeneous and stable microstructures, thereby achieving desired mechanical properties (Vilaro et al. 2011). However, prior experiments (Shiomi et al. 2004; Mur et al. 1996) are inconclusive in their optimal treatment temperatures. It is therefore critical to minimize residual stress *during* the fabrication process itself through careful optimization of processing parameters rather than relying solely on post-processing treatments. We discuss the thermal and mechanical models governing the manufacturing process next.

3.3 Thermal model

The governing equation for the heat transfer analysis in a powder bed fusion process (Zinoviev et al. 2016) is as follows:

$$\rho C_p(T)\frac{\partial T}{\partial t} = \nabla \cdot (\kappa(T)\nabla T) + Q_e, \tag{2}$$

where $T(x, y, z, t)$ is the temperature, ρ is the constant density of the material, $C_p(T)$ is the specific heat, $\kappa(T)$ is the thermal conductivity, and $Q_e(x, y, z, t)$ is the applied heat flux. The specific heat and thermal conductivity are modeled with second-degree polynomials as $C_p(T) = a_0 + a_1 T + a_2 T^2$ and $\kappa(T) = b_0 + b_1 T + b_2 T^2$, respectively. The parameters are specified in Sect. 5.1. The heat flux due to the electron beam, Q_e, can be modeled in a Gaussian form Fu and Guo (2014); Vastola et al. (2016):

$$Q_e(x, y, z, t; P, v, r, z_0) = \frac{2AP}{\pi r^2 z_0} \exp\left(-\frac{2\left((x-vt)^2 + y^2\right)}{r^2}\right) \times \frac{1}{5}\left[-3\left(\frac{z}{z_0}\right)^2 - 2\frac{z}{z_0} + 5\right], \tag{3}$$

where P is the beam power, v is the scanning speed, r is the beam spot radius, z_0 is the beam penetration depth, and A is the dimensionless powder absorptivity. The temperature history during the manufacturing process is used as the input to the mechanical model, as well as to obtain $T_{\max}$ in the constraint in (1) to ensure that the metal powder melts.

3.4 Mechanical model

The governing equation for mechanical analysis in a powder bed fusion process (Megahed et al. 2016) is given by

$$\nabla \cdot \boldsymbol{\sigma} + \mathbf{f} = \mathbf{0}, \tag{4}$$

where $\boldsymbol{\sigma}(x, y, z, t)$ denotes the stress tensor and $\mathbf{f}(x, y, z, t)$ are the internal forces that balance external forces. For the electron beam melting process, we first perform the thermal analysis as described above and the resulting temperature fields at every time instance drive the mechanical analysis to calculate stresses and strains. We perform mechanical analysis at every time instance.

The total strain is decomposed into elastic strain, plastic strain, and thermal strain, $\boldsymbol{\epsilon} = \boldsymbol{\epsilon}^e + \boldsymbol{\epsilon}^p + \boldsymbol{\epsilon}^t$. The elastic stress $\boldsymbol{\sigma}^e$ can be related to the elastic strain $\boldsymbol{\epsilon}^e$ through the rank-four elasticity tensor $\boldsymbol{C}$:

$$\boldsymbol{\sigma}^e = \boldsymbol{C}\boldsymbol{\epsilon}^e. \tag{5}$$

The plastic strain $\boldsymbol{\epsilon}^p$ is modeled by considering an elastic-perfectly plastic (Zhao et al. 2015) condition in the model. The thermal strain is calculated from the thermal expansion constitutive relationship: $\boldsymbol{\epsilon}^t = \alpha_t \Delta T$, where α_t is the thermal expansion coefficient. The presence of the thermal strain tensor ensures correct distortion calculation during the melting stage as well as the thermal shrinkage during the cooling stage (Megahed et al. 2016).

We choose the von Mises stress as the residual stress in the AM part. The von Mises stress is a function of the normal and shear stresses and is used to predict yielding of materials under complex loading. When the yield stress of the material is reached in the powder bed fusion process, plastic distortion occurs and the quality of the manufactured part is compromised.

In summary, we use the temperature history from the thermal model to compute the stress and strain in the mechanical model. The coupling between the two models is therefore uni-directional, as the mechanical response depends on the thermal response but not vice versa (Debroy et al. 2017).

3.5 Finite element model

The AM part of interest is shown in Fig. 2. The part's length is $l = 2$ mm, and the width and height are 1.5 mm and 0.65 mm, respectively. We use Ti–6Al–4V powder to manufacture this part. This alloy is commonly used in the aerospace and bioengineering industries because of its good mechanical properties, low density, and good corrosion resistance (Chastand et al. 2018).

We simulate the manufacturing of this part via an electron beam melting process in Abaqus using both thermal and mechanical finite element models. In electron beam melting, fused layers are stacked on top of each other; therefore, the layer thickness influences the resolution of the build (Cansizoglu et al. 2008). Early versions of electron beam melting process equipment used 100 μm as the standard layer thickness. The current standard layer thickness has been reduced to 50-70 μm (Karlsson et al. 2013). We use layer thickness of 50 μm here. In order to mitigate the computational cost of the finite element analysis, we only simulate the process of fusing the last powder layer (50 μm thick) to the bulk material formed by previous scans (0.6 mm high). We consider a single scan along the length in the x-direction through the powder layer on the top.

The inputs to the finite element model include the scanning speed v [mm/s], beam power P [W], preheating temperatures T_0 [°C], yield strength Y [MPa], elastic modulus E [GPa], bulk density ρ [kg/m^3], specific heat C_p [J/(kg·K)] and thermal conductivity κ [W/(m·K)]. Among these inputs, $C_p(T)$ and $\kappa(T)$ are functions of temperature

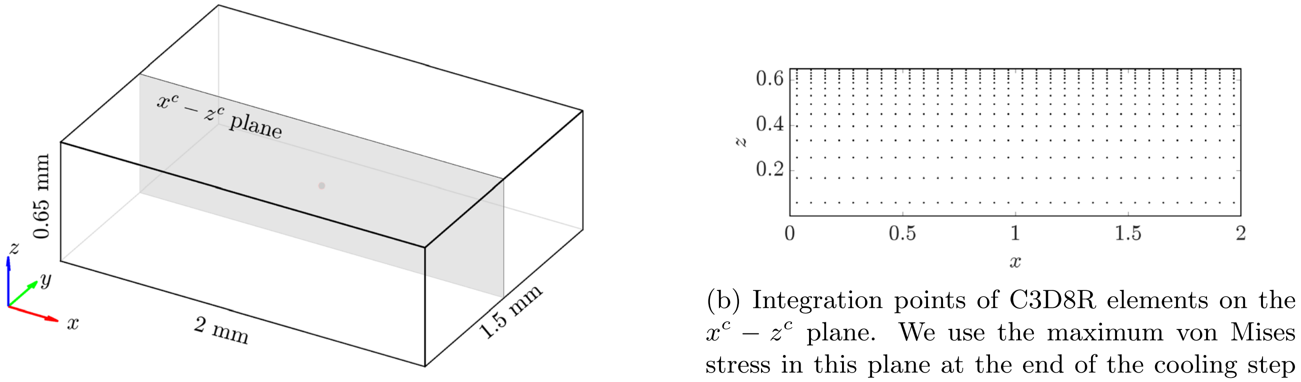

(a) Part geometry and the $x^c - z^c$ plane passing through the part centroid.

(b) Integration points of C3D8R elements on the $x^c - z^c$ plane. We use the maximum von Mises stress in this plane at the end of the cooling step to obtain $\sigma_{\max}$, the residual stress of interest.

Fig. 2 Part geometry and integration points on the $x^c - z^c$ plane and parameterized by polynomial coefficients, a_i and b_i, $i = 1, 2, 3$, respectively, as discussed in detail in Sect. 5.1. All values are converted to mm, MPa, and related units before being input into Abaqus.

We use three-node linear brick-type elements, specifically, DC3D8 (one degree of freedom per node, temperature) for the thermal model and C3D8R (24 degrees of freedom per element, $x, y,$ and z displacements) for the mechanical model. We use a non-uniform mesh, locally refined for the powder region where the heat flux is applied. We gradually coarsen the mesh for the rest of the part, which is indicated by the integration points corresponding to C3D8R elements intersecting the $x^c - z^c$ plane (the $x - z$ plane passing through the part centroid) in Fig. 2b. The mesh consists of 13,200 nodes and 10,752 elements in total. At each time instance, the thermal model has 13,200 degrees of freedom (DoFs) and the mechanical model has 39,600 DoFs.

In the thermal model, we allow the top surface to exchange heat with the surrounding through radiation. We model the radiation using the Stefan–Boltzmann law, $Q_r(x, y, z = 0.65\ \mathrm{mm}, t) = \sigma_{\mathrm{SB}}\epsilon_s(T^4(x, y, z = 0.65\ \mathrm{mm}, t) - T_c^4)$, where $\sigma_{\mathrm{SB}} = 5.67 \times 10^{-8}\ \mathrm{W \cdot m^{-2} \cdot K^{-4}}$ is the Stefan–Boltzmann constant, ϵ_s is the surface emissivity, and T_c is the constant chamber temperature. In the mechanical model, the boundary surfaces in the x-direction and y-direction are fixed in the x-coordinates and y-coordinates, respectively. The bottom surface is considered fixed in all coordinates. The finite element models based on the governing equations have been compared with experimental data in Vastola et al. (2016); Vohra et al. (2020).

There are four steps in the Abaqus models, namely laying powder, preheating, moving heat, and cooling. We simulate the process of laying the new powder on bulk material by activating the initially deactivated elements representing the powder layer. For our optimization problem (1), we extract $T_{\max}$ from the temperature history in step 3 (moving heat) and $\sigma_{\max}$ from the residual stress at the end of step 4 (cooling).

4 Solution to the risk-based design optimization problem

In this section, we present an efficient solution of the optimization problem formulated in Sect. 2. It is computationally prohibitive to obtain temperature history and residual stress for solving the design problem (1) using the high-fidelity finite element models described in Sects. 3.3 to 3.5, as the optimization process requires repeated model evaluations. To address this computational challenge, we construct surrogate models with training data obtained from the high-fidelity finite element models and solve the design optimization problem with surrogate models.

In Sect. 4.1, we introduce the risk measure, buffered probability of failure, used as a constraint in the design problem. Then, we discuss the surrogate modeling techniques for both thermal and mechanical finite element models in Sect. 4.2. In Sect. 4.3, we detail the solution of the design optimization problem with the integration of BPOF and surrogate models.

4.1 Buffered probability of failure (BPOF)

For an engineering system to be designed under uncertainty, we separate the inputs to the system into design variables $\mathbf{d} \in \mathcal{D} \subseteq \mathbb{R}^{N_d}$, random variables $Z \in \Omega$, and parameters $\boldsymbol{\theta} \in \Theta \subseteq \mathbb{R}^{N_\theta}$. Here, $\mathcal{D}$ is the design space, Ω is the space of random variables, Θ is the parameter space, and $\mathbb{R}$ represents the real numbers. A realization of Z is denoted by $z \in \mathbb{R}^{N_z}$.

We first introduce concepts related to buffered probability of failure, including probability of failure and superquantile. The failure of an engineering system can be described by the condition $g(\mathbf{d}, Z; \boldsymbol{\theta}) > \tau$, where $g : \mathcal{D} \times \Omega \times \Theta \to \mathbb{R}$ is the limit state function and $\tau \in \mathbb{R}$ is the failure threshold. For a system under uncertainty, $g(\mathbf{d}, Z; \boldsymbol{\theta})$ is a random variable given a particular design $\mathbf{d}$ and parameter $\boldsymbol{\theta}$. The probability of failure is defined as

$$p_\tau(g(\mathbf{d}, Z; \boldsymbol{\theta})) := \mathbb{P}[g(\mathbf{d}, Z; \boldsymbol{\theta}) > \tau]. \tag{6}$$

The POF is a measure of the set $\{g(\mathbf{d}, Z; \boldsymbol{\theta}) > \tau\}$, thus it does not include information about the magnitude of failure.

The α-quantile, Q_α, also known as the value-at-risk at level α, of the random variable $g(\mathbf{d}, Z; \boldsymbol{\theta})$ can be expressed as follows:

$$Q_\alpha[g(\mathbf{d}, Z; \boldsymbol{\theta})] := F^{-1}_{g(\mathbf{d}, Z; \boldsymbol{\theta})}(\alpha), \tag{7}$$

where $F^{-1}_{g(\mathbf{d}, Z; \boldsymbol{\theta})}(\cdot)$ is the inverse cumulative density function. Given a target reliability α_T, the corresponding target probability of failure is $1 - \alpha_T$, thus, POF and Q_{α_T} are related by

$$\begin{aligned} Q_{\alpha_T}[g(\mathbf{d}, Z; \boldsymbol{\theta})] < \tau \quad &\Leftrightarrow \quad p_\tau(g(\mathbf{d}, Z; \boldsymbol{\theta})) < 1 - \alpha_T, \\ Q_{\alpha_T}[g(\mathbf{d}, Z; \boldsymbol{\theta})] = \tau \quad &\Leftrightarrow \quad p_\tau(g(\mathbf{d}, Z; \boldsymbol{\theta})) = 1 - \alpha_T, \\ Q_{\alpha_T}[g(\mathbf{d}, Z; \boldsymbol{\theta})] > \tau \quad &\Leftrightarrow \quad p_\tau(g(\mathbf{d}, Z; \boldsymbol{\theta})) > 1 - \alpha_T, \end{aligned} \tag{8}$$

as shown in Fig. 3.

The α-superquantile, $\bar{Q}_\alpha$, also know as conditional value-at-risk at level α, is defined based on the α-quantile Q_α:

$$\begin{aligned} \bar{Q}_\alpha[g(\mathbf{d}, Z; \boldsymbol{\theta})] &:= Q_\alpha[g(\mathbf{d}, Z; \boldsymbol{\theta})] \\ &+ \frac{1}{1 - \alpha}\mathbb{E}\left[\left[g(\mathbf{d}, Z; \boldsymbol{\theta}) - Q_\alpha[g(\mathbf{d}, Z; \boldsymbol{\theta})]\right]^+\right], \end{aligned} \tag{9}$$

where $[c]^+ := \max\{0, c\}$. The conditional value-at-risk is a tail expectation, i.e., an average over the portion exceeding the failure threshold. It is the sum of the α-quantile and a non-negative term and is thus conservative compared to the

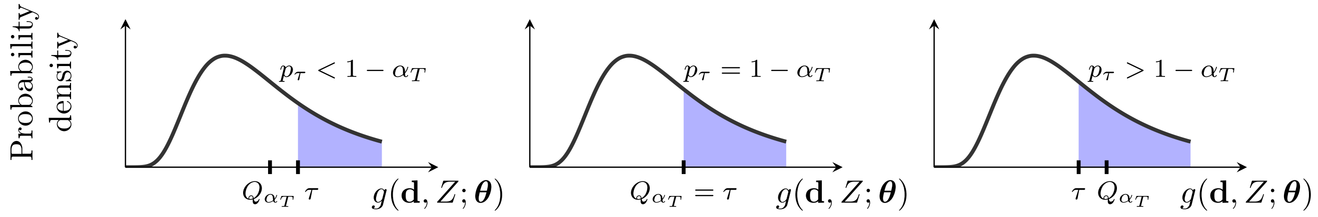

Fig. 3 Relationship between the probability of failure (shaded area under the pdf curve) and α-quantile

α-quantile. By definition, $\bar{Q}_0[g(\mathbf{d}, Z;\boldsymbol{\theta})] = \mathbb{E}[g(\mathbf{d}, Z;\boldsymbol{\theta})]$ and $\bar{Q}_1[g(\mathbf{d}, Z;\boldsymbol{\theta})]$ is the essential supremum of $g(\mathbf{d}, Z;\boldsymbol{\theta})$.

The buffered probability of failure is an alternative measure of reliability/risk that adds a buffer to the POF. The BPOF is defined based on the superquantile as

$$\bar{p}_\tau(g(\mathbf{d}, Z;\boldsymbol{\theta})) := \begin{cases} \{1-\alpha \mid \bar{Q}_\alpha[g(\mathbf{d}, Z;\boldsymbol{\theta})] = \tau\}, & \text{if } \bar{Q}_0[g(\mathbf{d}, Z;\boldsymbol{\theta})] < \tau < \bar{Q}_1[g(\mathbf{d}, Z;\boldsymbol{\theta})], \\ 0, & \text{if } \tau \geq \bar{Q}_1[g(\mathbf{d}, Z;\boldsymbol{\theta})], \\ 1, & \text{otherwise.} \end{cases} \tag{10}$$

Note that by definition, $\mathbb{P}\left[g(\mathbf{d}, Z;\boldsymbol{\theta}) \geq Q_\alpha[g(\mathbf{d}, Z;\boldsymbol{\theta})]\right] = 1-\alpha$, thus the first condition in (10) is

$$\bar{p}_\tau(g(\mathbf{d}, Z;\boldsymbol{\theta})) = \mathbb{P}\left[g(\mathbf{d}, Z;\boldsymbol{\theta}) \geq Q_\alpha[g(\mathbf{d}, Z;\boldsymbol{\theta})]\right], \tag{11}$$

where α satisfies $\bar{Q}_\alpha[g(\mathbf{d}, Z;\boldsymbol{\theta})] = \tau$. The BPOF can be viewed as the probability of exceeding a quantile given the target reliability level α. Alternatively, the BPOF can be written in the form of an expectation as

$$\bar{p}_\tau(g(\mathbf{d}, Z;\boldsymbol{\theta})) = \min_{\zeta<\tau} \frac{\mathbb{E}\left[[g(\mathbf{d}, Z;\boldsymbol{\theta}) - \zeta]^+\right]}{\tau - \zeta}, \tag{12}$$

where ζ is an auxiliary variable, and the optimum ζ^* is the threshold from (11) that provides $\mathbb{E}[g(\mathbf{d}, Z;\boldsymbol{\theta}) | g(\mathbf{d}, Z;\boldsymbol{\theta}) > \zeta^*] = \tau$. This form of BPOF assumes that $\bar{Q}_0[g(\mathbf{d}, Z;\boldsymbol{\theta})] < \tau < \bar{Q}_1[g(\mathbf{d}, Z;\boldsymbol{\theta})]$ and $g(\mathbf{d}, Z;\boldsymbol{\theta})$ is integrable. The BPOF in (11) can be further split into a sum of a non-negative term and POF as

$$\begin{aligned} \bar{p}_\tau(g(\mathbf{d}, Z;\boldsymbol{\theta})) &= \mathbb{P}\left[g(\mathbf{d}, Z;\boldsymbol{\theta}) \in [Q_\alpha[g(\mathbf{d}, Z;\boldsymbol{\theta})], \tau]\right] + \mathbb{P}[g(\mathbf{d}, Z;\boldsymbol{\theta}) > \tau] \\ &= \mathbb{P}\left[g(\mathbf{d}, Z;\boldsymbol{\theta}) \in [\zeta, \tau]\right] + p_\tau(g(\mathbf{d}, Z;\boldsymbol{\theta})), \end{aligned} \tag{13}$$

where $\zeta = Q_\alpha[g(\mathbf{d}, Z;\boldsymbol{\theta})]$ depends on α through the superquantile.

Note that the probability of failure is an intuitive risk measure as it simply measures the failure frequency. By comparison, the buffered probability of failure accounts for both the frequency *and* magnitude of failure through the first term in (13). The conservativeness of BPOF stems from the selection of the threshold $\zeta \leq \tau$ based on data. When realizations of $g(\mathbf{d}, Z;\boldsymbol{\theta})$ beyond τ are large (corresponding to potentially catastrophic failures), ζ has to be smaller to drive the expectation beyond ζ to τ thus making BPOF bigger. Since the ζ-tail is on average equal to τ, when there are a large number of near-failure events, the near-failure region $[\zeta, \tau]$ is determined by the frequency and magnitude of tail events around τ. This can be intuitively viewed as a buffer to the POF as shown in Fig. 4.

We further note that the probability of failure $p_\tau(g(\mathbf{d}, Z;\boldsymbol{\theta}))$, defined in (6), measures the failure set but is not necessarily convex in the design variables $\mathbf{d}$. In contrast, the superquantile $\bar{Q}_\alpha[g(\mathbf{d}, Z;\boldsymbol{\theta})]$, defined in (9), is convex in $\mathbf{d}$ when $g(\mathbf{d}, Z;\boldsymbol{\theta})$ is convex in $\mathbf{d}$, since $[\cdot]^+$ is a convex function. Similarly, the BPOF $\bar{p}_\tau(g(\mathbf{d}, Z;\boldsymbol{\theta}))$, defined in (12), forms a convex optimization problem. Unlike traditional reliability-based design optimization problems, where convexity is not preserved due to the non-convex nature of the probability of failure, incorporating BPOF as a constraint maintains convexity with respect to $\mathbf{d}$. This convexity ensures convergence to a global optimal design when using standard, efficient optimization algorithms. Moreover, when the probability of failure is non-differentiable with respect to $\mathbf{d}$, estimating POF gradients can be ill-conditioned,

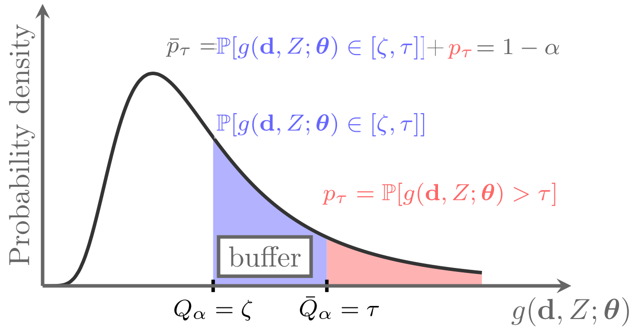

Fig. 4 BPOF $\bar{p}_\tau$ illustration at threshold τ: BPOF equals POF plus the buffer

posing challenges for gradient-based optimizers that depend on accurate gradient evaluations.

We can use a sampling-based approach, see Algorithm 1, to estimate the α-quantile Q_α, α-superquantile $\bar{Q}_\alpha$, and BPOF $\bar{p}_\tau$ as Q_α and $\bar{Q}_\alpha$ can be viewed as expectations. With m Monte Carlo samples, the estimation errors decrease at a rate of $1/\sqrt{m}$ and the estimator variance increases with larger α values.

Algorithm 1 Sampling-based estimations of Q_α, $\bar{Q}_\alpha$, and $\bar{p}_\tau$

```
Input $m$ i.i.d. samples $\boldsymbol{z}_1, \dots, \boldsymbol{z}_m$ of random variable $Z$; design variable $\mathbf{d}$; parameters $\boldsymbol{\theta}$; risk level $\alpha \in (0, 1)$.
Output Sample approximations $\widehat{Q}_\alpha[g(\mathbf{d}, Z; \boldsymbol{\theta})]$, $\widehat{\bar{Q}}_\alpha[g(\mathbf{d}, Z; \boldsymbol{\theta})]$, and $\widehat{p}_\tau(g(\mathbf{d}, Z; \boldsymbol{\theta}))$.
Evaluate limit state function at the samples to get $g(\mathbf{d}, \boldsymbol{z}_1; \boldsymbol{\theta}), \dots, g(\mathbf{d}, \boldsymbol{z}_m; \boldsymbol{\theta})$.
Sort values of limit state function in descending order and relabel the samples so that
    $$g(\mathbf{d}, \boldsymbol{z}_1; \boldsymbol{\theta}) > g(\mathbf{d}, \boldsymbol{z}_2; \boldsymbol{\theta}) > \cdots > g(\mathbf{d}, \boldsymbol{z}_m; \boldsymbol{\theta}).$$
$\widehat{Q}_\alpha[g(\mathbf{d}, Z; \boldsymbol{\theta})] \leftarrow g(\mathbf{d}, \boldsymbol{z}_{k_\alpha}; \boldsymbol{\theta})$, where $k_\alpha = m(1 - \alpha)$.
Estimate $\widehat{\bar{Q}}_\alpha[g(\mathbf{d}, Z; \boldsymbol{\theta})]$ using (9).
$c = g(\mathbf{d}, \boldsymbol{z}_1; \boldsymbol{\theta})$.
$k = 1$.
while $c \geq \widehat{\bar{Q}}_\alpha[g(\mathbf{d}, Z; \boldsymbol{\theta})]$ do
    $k \leftarrow k + 1$.
    $c = \frac{1}{k} \sum_{i=1}^{k} g(\mathbf{d}, \boldsymbol{z}_k; \boldsymbol{\theta})$.
end while
Estimate BPOF as $\widehat{p}_\tau(g(\mathbf{d}, Z; \boldsymbol{\theta})) \approx \frac{k-1}{m}$, $\tau \approx c$.
```

4.2 Surrogate modeling techniques

We use surrogate models to approximate the FEM solutions and accelerate the optimization. Here, we discuss the surrogate modeling techniques for both the thermal and mechanical models.

The temperature history in additive manufacturing processes exhibits strong temporal correlation, while residual stress exhibits spatial correlation in the printed part. We use an efficient approach to transform these correlated high-dimensional outputs into an uncorrelated feature space, which enables separate surrogate modeling of features as discussed below. Specifically, we first map temperature histories and residual stresses to features (see Sect. 4.2.1 for details) in uncorrelated spaces using singular value decomposition (SVD). We then identify the active subspaces of the input variables and construct surrogate models of features versus their corresponding active variables in the active subspace. This strategy achieves effective dimension reduction for both the inputs and the quantities of interest (QoIs), which enables efficient modeling for the complex physical phenomena inherent in the additive manufacturing process. Finally, we use surrogate model predictions of features and SVD components to recover the temperature histories and residual stress, which are used in the optimization formulation.

4.2.1 Singular value decomposition for feature generation

We model the manufacturing process by the design vector $\mathbf{d}$, the random vector Z, and the deterministic parameters $\boldsymbol{\theta}$ as discussed in Sect. 2. To obtain training data for the surrogate models, we generate M random samples of *both* the design variables and random variables. We denote $\Xi = [v, P, T_0, Y, E, \rho]^\top$ as a random variable and a realization of Ξ as $\boldsymbol{\xi}$. We obtain both the thermal and mechanical FEM outputs corresponding to each sample $\boldsymbol{\xi}_i$, $i = 1, 2, \dots, M$, and reshape the FEM outputs corresponding to each sample as a row vector of length N. We then assemble these vectors into a matrix $\mathbf{F} \in \mathbb{R}^{M \times N}$.

The singular value decomposition of $\mathbf{F} \in \mathbb{R}^{M \times N}$ is $\mathbf{F} = \mathbf{U}\boldsymbol{\Sigma}\mathbf{V}' = \sum_{k=1}^{\min(M,N)} \sigma_k \mathbf{u}_k \mathbf{v}_k'$, where $\mathbf{U} \in \mathbb{R}^{M \times M}$ and $\mathbf{V} \in \mathbb{R}^{N \times N}$ are unitary matrices that have the left singular vectors $\mathbf{u}_k$ and right singular vector $\mathbf{v}_k$ as columns, respectively. The diagonal matrix $\boldsymbol{\Sigma} \in \mathbb{R}^{M \times N}$ contains singular values $\sigma_1, \sigma_2, \dots, \sigma_p$, $p = \min\{M, N\}$ which are ordered by magnitude, $\sigma_1 \geq \sigma_2 \geq \dots \geq \sigma_p \geq 0$.

The best approximation in the least-squares sense of the data matrix $\mathbf{F}$ can be obtained by $\hat{\mathbf{F}} = \mathbf{U}_k \boldsymbol{\Sigma}_k \mathbf{V}_k'$, where $\mathbf{U}_k$ is a matrix containing the first k left singular vector, $\boldsymbol{\Sigma}_k$ is the first k singular values organized in a $k \times k$ diagonal matrix, and $\mathbf{V}_k$ is a matrix containing the first k right singular vectors. We denote the product of the matrices $\mathbf{U}_k$ and $\boldsymbol{\Sigma}_k$ as follows:

$$\mathcal{F} = \mathbf{U}_k \boldsymbol{\Sigma}_k \in \mathbb{R}^{M \times k}, \tag{14}$$

which induces a factorization of $\hat{\mathbf{F}}$. Due to the orthonormality of $\mathbf{V}$ in the SVD, $\mathcal{F}$ has the following properties: (a) each row $\mathcal{F}_{i,:}$ can be viewed as a k-dimensional coordinate on the orthonormal basis $[\mathbf{v}_1, \mathbf{v}_2, \dots, \mathbf{v}_k] =: \mathbf{V}[:, 1 : k]$. Any two components in the coordinate, $\mathcal{F}_{i,j}$, and $\mathcal{F}_{i,m}$, $j \neq m$, are uncorrelated. We refer to $\mathcal{F}_{i,j}$, the coordinate component in $\mathcal{F}_{i,:}$ that is indexed by j, as a realization of *feature* j. (b) The mapping between $\mathcal{F}$ and $\hat{\mathbf{F}}$ is exact with the knowledge of $\mathbf{V}_k$:

$$\hat{\mathbf{F}} = \mathcal{F}\mathbf{V}_k'. \tag{15}$$

When $k = N$, this becomes $\mathbf{F} = \mathcal{F}\mathbf{V}'$.

In summary, the original data in $\mathbf{F}$ can be approximated with k features, $\mathcal{F}_{:,1}, \mathcal{F}_{:,2}, \dots, \mathcal{F}_{:,k}$, in $\mathcal{F}$ and the first k right singular vectors of $\mathbf{F}$. These features, corresponding to the first k left singular vectors and singular values, are uncorrelated. When k is smaller than N, dimension reduction is achieved.

4.2.2 Active subspace discovery and active variable calculation

An active subspace is a low-dimensional subspace that consists of important directions in a model's input space (Constantine 2015). Most of the variability in the output due to the uncertain inputs is captured along these important directions. In the design optimization problem, we are interested in discovering the active subspace related to the features corresponding to the thermal and mechanical model outputs. Every feature column $\mathcal{F}_{:,j}$ can be treated as a scalar-valued function of the input $\boldsymbol{\xi}$, $\mathcal{F}_{:,j}(\boldsymbol{\xi})$. An active subspace is thus a low-dimensional subspace in the input domain that effectively captures the variability in $\mathcal{F}_{:,j}$ due to variations in $\boldsymbol{\xi}$.

The directions constituting the active subspace are the dominant eigenvectors of the covariance matrix $\mathcal{C} = \int_\Omega \left(\nabla_\Xi \mathcal{F}_{:,j}\right)\left(\nabla_\Xi \mathcal{F}_{:,j}\right)^\top \pi(\boldsymbol{\xi}) \mathrm{d}\boldsymbol{\xi}$, where $\pi(\boldsymbol{\xi})$ is the joint probability density function of Ξ. The eigenvalue decomposition of the matrix $\mathcal{C}$ is given by $\mathcal{C} = \mathbf{W}\boldsymbol{\Lambda}\mathbf{W}^{'}$. Since $\mathcal{C}$ is real, symmetric and positive semidefinite, its eigenvalues are non-negative real values and its eigenvectors are orthogonal. Thus, the eigenvector matrix and eigenvalue matrix can be partitioned about the rth eigenvalue such that there is a significant drop in magnitude, i.e., $\lambda_r / \lambda_{r+1} \gg 1$ as

$$\mathbf{W} = \left[\mathbf{W}_1 \ \mathbf{W}_2\right], \quad \boldsymbol{\Lambda} = \begin{bmatrix} \boldsymbol{\Lambda}_1 & \\ & \boldsymbol{\Lambda}_2 \end{bmatrix}. \tag{16}$$

The columns of $\mathbf{W}_1 = [\mathbf{w}_1, \mathbf{w}_2, \dots, \mathbf{w}_r]$ span the dominant eigenspace of $\mathcal{C}$ and the active subspace and the corresponding active variable is calculated as $\boldsymbol{\eta} = \mathbf{W}_1^{'}\xi \in \mathbb{R}^r$. When r is smaller than the dimension of Ξ, dimension reduction is achieved.

We use the trained surrogate models to estimate feature values for unseen model inputs, including design variables, random variables, and system parameters. We then use the right singular vector matrix $\mathbf{V}$ of the SVD to obtain the temperature history and residual stress estimations corresponding to the unseen input using (15). These estimations are used in the optimization problem (1). We only compute surrogate models for $K_\mathcal{T}$ features of the temperature history and $K_\mathcal{S}$ features of the residual stress. We discuss the details of surrogate model constructions in Sects. 4.2.3 and 4.2.4.

4.2.3 Surrogate model for temperature history

In the optimization setup (1), the constraint on temperature history ensures the powder properly melts. Since we model a single scan along the length at the top surface of the part as discussed in Sect. 3, we choose to record the temperature history at the centroid of the top surface of the part. The total scan time $t_\mathrm{scan} = l/v$ varies between simulations with different scanning speeds.

Since the beam moves at constant velocity, the temperature is expected to peak at approximately $0.5 \cdot t_\mathrm{scan}$. We take temperature measurements at selected non-uniform time instances within $[0, t_\mathrm{scan}]$ according to the following distribution: (a) ten uniformly spaced measurements, $T_1, T_2, \dots, T_{10}$, in the interval $[0, 0.405 \cdot t_\mathrm{scan}]$; (b) ten uniformly spaced measurements, $T_{11}, T_{12}, \dots, T_{20}$, in the interval $[0.45 \cdot t_\mathrm{scan}, 0.54 \cdot t_\mathrm{scan}]$; and (c) eleven uniformly spaced measurements, $T_{21}, T_{22}, \dots, T_{31}$, in the interval $[0.55 \cdot t_\mathrm{scan}, t_\mathrm{scan}]$. Note that we use an increased sampling density within $[0.45 \cdot t_\mathrm{scan}, 0.54 \cdot t_\mathrm{scan}]$ to ensure precise capture of the maximum temperature at the center of the part's top surface.

With $\mathcal{M}$ simulations, we compile a snapshot matrix $\mathbf{T} \in \mathbb{R}^{\mathcal{M} \times 31}$. Each row in the snapshot matrix, $\mathbf{T}_{i,:}$, contains the temperatures at thirty-one time instances $[T_1, T_2, \dots, T_{31}]$ of simulation i, where $i = 1, 2, \dots, \mathcal{M}$. We apply an SVD and active subspace discovery, as detailed in Sects. 4.2.1 and 4.2.2, to extract features $\mathcal{T}$ and corresponding active variables $\boldsymbol{\eta}_{(\mathbf{T})}$. We select the most significant $K_\mathcal{T}$ features to construct surrogate models $\hat{G}_{\mathcal{T}_{:,j}}(\boldsymbol{\eta}_{(j_\mathrm{T})}) \approx \mathcal{T}_{:,j}((\mathbf{d}, Z; \boldsymbol{\theta}))$ for $j = 1, 2, \dots, K_\mathcal{T}$.

We choose $K_\mathcal{T}$ based on prediction error on the training data, see Sect. 5.2.1 for a detailed discussion.

4.2.4 Surrogate model for residual stress

We measure the residual stress on the non-uniform grid comprising 32 points along the length and 14 points along the height on the $x^c - z^c$ plane, as shown in Fig. 2b. We use the maximum von Mises stress measured at the end of the cooling step in this plane as the residual stress of interest.

Each simulation generates a comprehensive stress field $\boldsymbol{\sigma} \in \mathbb{R}^{32\times 14}$ for the $x^c - z^c$ plane. For a set of $\mathcal{M}$ simulations, we vectorize the stress fields and consolidate them into a matrix $\mathbf{S} \in \mathbb{R}^{\mathcal{M}\times 448}$. We then apply an SVD and active subspace discovery, as discussed in Sects. 4.2.1 and 4.2.2, to obtain features $\mathcal{S}$ and corresponding active variables $\boldsymbol{\eta}_{(\mathbf{S})}$. We select the most influential $K_\mathcal{S}$ features to construct surrogate models $\hat{G}_{\mathcal{S}_{:,j}}(\boldsymbol{\eta}_{(j_\mathrm{S})}) \approx \mathcal{S}_{:,j}((\mathbf{d}, Z;\boldsymbol{\theta}))$ for $j = 1, 2, ..., K_\mathcal{S}$. Similar to the thermal case discussed above, we choose $K_\mathcal{S}$ based on prediction error on the training data, see Sect. 5.2.2 for a detailed discussion.

4.3 Optimization problem solution

We follow a two-phase process to solve the design optimization under uncertainty problem. In phase 1, we construct uncorrelated surrogate models by performing singular value decompositions on the QoIs and active subspace discoveries on their corresponding inputs. In phase 2, we run the optimization iterations, where we use the trained surrogate models in phase 1 to expedite the computation. This two-phase process is, in principle, generalizable to many other design optimization under uncertainty problems, with modifications to parameters of the surrogate model on a case-by-case basis.

We reformulate the original optimization problem (1) as a problem with an expectation in the constraint on residual stress:

$$
\begin{aligned}
\min_{\substack{P_L \le P \le P_U,\\ v_L \le v \le v_U,\\ \zeta < \tau}} \quad & P \cdot \frac{l}{v} \\
\text{subject to} \quad & \frac{\mathbb{E}\left[[\sigma_{\max}(\mathbf{d}, Z;\boldsymbol{\theta}) - \zeta]^+\right]}{\tau - \zeta} \le 1 - \alpha_T, \\
& T_{\mathrm{liq}} < T_{\max}(\mathbf{d}, Z;\boldsymbol{\theta}) < 1.1 \times T_{\mathrm{liq}},
\end{aligned}
\tag{17}
$$

where ζ is an auxiliary variable and τ is the failure threshold related to the reliability level α as discussed in Sect. 4.1. We solve the optimization problem (17) by following the steps outlined in Algorithms 2.1 and 2.2, where we also include additional details on the surrogate models of the temperature history and residual stress.

Algorithm 2.1 Solution to the risk-based design optimization (17)

```
Phase 1 - Surrogate model constructions
Generate $\mathcal{M}$ samples of $\mathbf{d}$, $\boldsymbol{d}_1, \dots, \boldsymbol{d}_\mathcal{M}$, and realizations of $Z$, $\boldsymbol{z}_1, \dots, \boldsymbol{z}_\mathcal{M}$; denote $\boldsymbol{\xi}_i = [\boldsymbol{d}_i^\top, \boldsymbol{z}_i^\top]^\top$.
Perform FEM simulations using $[\boldsymbol{\xi}_i^\top; \boldsymbol{\theta}^\top]^\top, i = 1, 2, \dots, \mathcal{M}$, as inputs and obtain the temperature snapshot matrix $\mathbf{T}$ and residual stress matrix $\mathbf{S}$.
Perform an SVD $\mathbf{T} = \mathbf{U_T \Sigma_T V'_T}$.
Select $K_\mathcal{T}$ features, $\mathcal{T}_{:,1}, \mathcal{T}_{:,2}, \dots, \mathcal{T}_{:,K_\mathcal{T}}$.
for $j_\mathbf{T} = 1, 2, \dots, K_\mathcal{T}$ do
    Perform an active subspace discovery to find the matrix $\mathbf{W}_{1(j_\mathbf{T})}$.
    Construct surrogate model $\hat{G}_{\mathcal{T}_{:,j_\mathbf{T}}}$ with training data set $\left\{\left(\mathbf{W}_{1(j_\mathbf{T})}^\top \cdot \boldsymbol{\xi}_i,\ \mathcal{T}_{i,j_\mathbf{T}}\right)\right\}_{i=1}^{\mathcal{M}}$.
end for
Perform an SVD $\mathbf{S} = \mathbf{U_S \Sigma_S V'_S}$.
Select $K_\mathcal{S}$ features, $\mathcal{S}_{:,1}, \mathcal{S}_{:,2}, \dots, \mathcal{S}_{:,K_\mathcal{S}}$.
for $j_\mathbf{S} = 1, 2, \dots, K_\mathcal{S}$ do
    Perform an active subspace discovery to find the matrix $\mathbf{W}_{1(j_\mathbf{S})}$.
    Construct surrogate model $\hat{G}_{\mathcal{S}_{:,j_\mathbf{T}}}$ with training data set $\left\{\left(\mathbf{W}_{1(j_\mathbf{S})}^\top \cdot \boldsymbol{\xi}_i,\ \mathcal{S}_{i,j_\mathbf{S}}\right)\right\}_{i=1}^{\mathcal{M}}$.
end for
```

Algorithm 2.2 Solution to the risk-based design optimization (17)

```
Phase 2 - Optimization iterations
Initialize: Set $\mathbf{d} = \mathbf{d}^{\{0\}}$, $i = 1$.
while not converged do
    Generate $\mathcal{N}$ samples of $Z$, $\boldsymbol{z}_1, \boldsymbol{z}_2, \ldots, \boldsymbol{z}_{\mathcal{M}}$.
    for $k = 1, 2, \ldots, \mathcal{N}$ do
        for $j_{\mathbf{T}} = 1, 2, \ldots, K_{\mathcal{T}}$ do
            Calculate active variable $\boldsymbol{\eta}_{k(j_{\mathbf{T}})} = \mathbf{W}^{\top}_{1(j_{\mathbf{T}})} \cdot \boldsymbol{\xi}_k$, where $\boldsymbol{\xi}_k = [\mathbf{d}^{\top}, \boldsymbol{z}_j^{\top}]^{\top}$.
            Calculate feature value $\hat{G}_{\mathcal{T}_{:,1}}(\boldsymbol{\eta}_{k(j_{\mathbf{T}})})$.
        end for
        Estimate temperature snapshot $\hat{\mathbf{T}}_{k,:} \in \mathbb{R}^{1\times 31}$, (the $k$-th row of matrix $\hat{\mathbf{T}}$) as
            $$\hat{\mathbf{T}}_{k,:} = [\hat{G}_{\mathcal{T}_{:,1}}, \hat{G}_{\mathcal{T}_{:,1}}, \ldots, \hat{G}_{\mathcal{T}_{:,K_{\mathcal{T}}}}] \cdot \mathbf{V}_{\mathbf{T}}\,[:, 1 : K_{\mathcal{T}}]^{\top} .$$
        Find the maximum temperature $\hat{T}_{k,\max} = \max\{\hat{\mathbf{T}}_{j,:}\}$.
        for $j_{\mathbf{S}} = 1, 2, \ldots, K_{\mathcal{S}}$ do
            Calculate active variable $\boldsymbol{\eta}_{k(j_{\mathbf{S}})} = \mathbf{W}^{\top}_{1(j_{\mathbf{S}})} \cdot \boldsymbol{\xi}_k$.
            Calculate feature value $\hat{G}_{\mathcal{S}_{:,1}}(\boldsymbol{\eta}_{k(j_{\mathbf{S}})})$.
        end for
        Estimate residual stress $\hat{\mathbf{S}}_{k,:} \in \mathbb{R}^{1\times 448}$, (the $j$-th row of matrix $\hat{\mathbf{S}}$) as
            $$\hat{\mathbf{S}}_{k,:} = [\hat{G}_{\mathcal{S}_{:,1}}, \hat{G}_{\mathcal{S}_{:,1}}, \ldots, \hat{G}_{\mathcal{S}_{:,K_{\mathcal{S}}}}] \cdot \mathbf{V}_{\mathbf{S}}\,[:, 1 : K_{\mathcal{S}}]^{\top} . \tag{18}$$
        Find the maximum residual stress $\hat{\sigma}_{k,\max} = \max\{\hat{\mathbf{S}}_{k,:}\}$.
    Estimate $T_{\max}$ as $\hat{T}_{\max} = \frac{1}{\mathcal{N}} \sum_{k=1}^{\mathcal{N}} \hat{T}_{k,\max}$.
    end for
    Use the estimated $\hat{T}_{\max}$ and $k$ realizations of $\hat{\sigma}_{\max}$ in (17) in an optimization solver for $\mathbf{d}^{\{i\}}$.
    $\mathbf{d} \leftarrow \mathbf{d}^{\{i\}}$, $i \leftarrow i + 1$.
end while
Return: Set solution $\mathbf{d}^{*} = \mathbf{d}^{\{i\}}$.
```

5 Numerical results

We present the numerical results in this section. In Sect. 5.1, we outline the numerical setup for implementing the finite element simulations. We show surrogate model details and optimization results in Sect. 5.2 and Sect. 5.3, respectively. Finally, we validate the optimized results in Sect. 5.4 and compare them with those of a more traditional reliability-based design optimization formulation in Sect. 5.5.

5.1 Simulation setup

The set of process parameters includes scanning speed (v), beam power (P), and preheating temperature (T_0). Mechanical properties include yield strength (Y), elastic modulus (E), and bulk density (ρ). Thermal properties include specific heat (C_p) and bulk thermal conductivity (κ). As discussed in Sect. 2, $\mathbf{d} = [v, P]^{\top}$ contains the design variables and $Z = [T_0, Y, E, \rho]^{\top}$ is the vector of random variables. The upper and lower bounds of the design variables are $v_L = 100$ mm/s, $v_U = 1{,}000$ mm/s, $P_L = 20$ W, and $P_U = 200$ W. The bounds on the random variables are listed in Table 1. We use uniform distributions for all random variables. We choose the distribution type and supports based on (Vohra et al. (2020), Sect. 4.1). The parameter vector $\boldsymbol{\theta} \in \mathbb{R}^6$ consists of six coefficients, a_i and b_i, $i = 1, 2, 3$, for calculating the specific heat $C_p(T) = a_0 + a_1 T + a_2 T^2$ and the thermal conductivity $\kappa(T) = b_0 + b_1 T + b_2 T^2$, respectively. We determine the six coefficients using data from Fu and Guo (2014) and their values are as follows: $a_0 = 540$ J/(kg·K), $a_1 = 0.43$ J/(kg·K^2), $a_2 = -3.2 \times 10^{-5}$ J/(kg·K^3), $b_0 = 7.2$ W/(m·K), $b_1 = 0.011$ W/(m·K^2), and $b_2 = 1.4 \times 10^{-6}$ W/(m·K^3).

Table 1 Uniform random variables used in the additive manufacturing example

Random variable	Lower bound	Upper bound
T_0 [°C]	585	715
Y [MPa]	742.5	907.5
E [GPa]	100	120
ρ [kg/m^3]	3870	4730

The constant chamber temperature is $T_c = 650$ °C in the thermal model.

As discussed in Sect. 3.5, the finite element simulations use Ti–6Al–4V powder and it is characterized by the following properties (Welsch et al. 1993). The bulk density is 4,428kg/m^3, powder density is 2,700kg/m^3, solidus temperature is 1,605°C, liquidus temperature is $T_{\text{liq}} = 1{,}650$°C, elastic modulus is $E = 110$ GPa, Poisson's ratio is 0.41, yield strength is $Y = 825$ MPa, surface emissivity is $\epsilon_s = 0.35$, powder absorptivity is $A = 0.203$, and the thermal expansion coefficient is $\alpha_t = 1 \times 10^{-5}$. The latent heat of fusion is 365,000J/kg, which represents the energy required to transition from solid to liquid phase without a change in temperature. To simplify calculation, we use a constant density value $\rho = 4{,}300$ kg/m^3, the volume-averaged density of powder and bulk alloy. We use a total of 120 training samples ($\mathcal{M} = 120$ in Algorithm 2.1) of $(\mathbf{d}, Z)$, generated using optimal symmetric Latin hypercube sampling in the space $\mathcal{D} \times \Omega$, to train the surrogate models $\hat{G}_{\mathcal{T}_{:,j}}(\boldsymbol{\eta}_{(j_{\mathbf{T}})})$ and $\hat{G}_{\mathcal{S}_{:,j}}(\boldsymbol{\eta}_{(j_{\mathbf{S}})})$.

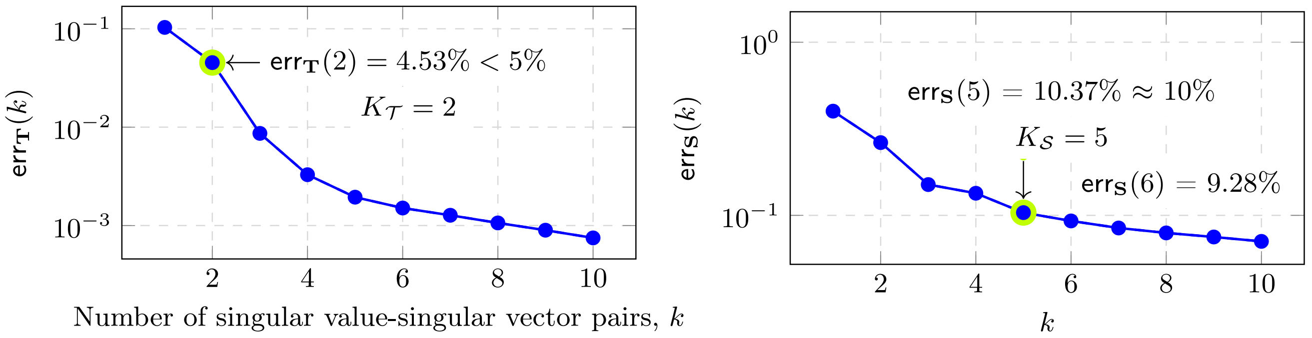

(a) Temperature snapshots. (b) Residual stress.

Fig. 5 The mean relative error between (a) temperature snapshots or (b) residual stress and their corresponding approximations using k singular value–singular vector pairs. We choose (a) $K_{\mathcal{S}}$ or (b) $K_{\mathcal{T}}$ features for which we build surrogate models based on the error

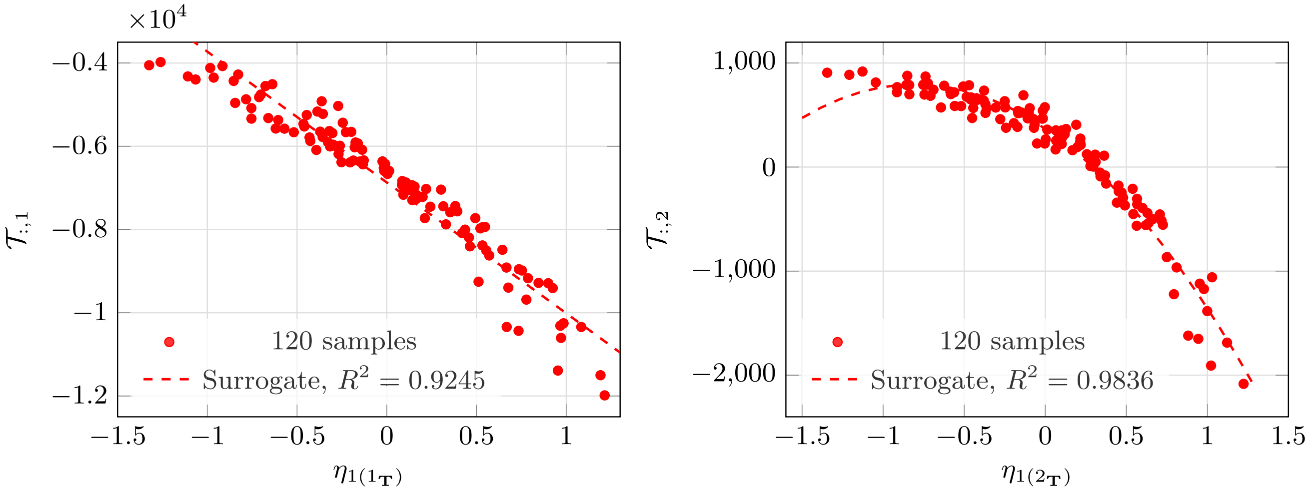

(a) Feature 1. (b) Feature 2.

Fig. 6 Surrogate models for the two features of the temperature data

Table 2 Surrogate models for features 1 to 5 of residual stress, $\hat{G}_{\mathcal{S}_{:,1}}$ to $\hat{G}_{\mathcal{S}_{:,5}}$

Surrogate	Number of active variables	Polynomial type	R^2 value
$\hat{G}_{\mathcal{S}_{:,1}}$	1	Parabola	0.9665
$\hat{G}_{\mathcal{S}_{:,2}}$	2	Fifth-degree polynomial surface	0.9074
$\hat{G}_{\mathcal{S}_{:,3}}$	2	Fifth-degree polynomial surface	0.8869
$\hat{G}_{\mathcal{S}_{:,4}}$	3	Sixth-degree polynomial surface	0.8118
$\hat{G}_{\mathcal{S}_{:,5}}$	2	Fifth-degree polynomial surface	0.8493

5.2 Surrogate models

5.2.1 Temperature snapshot surrogate model

We perform an SVD on $\mathbf{T} \in \mathbb{R}^{120\times 31}$ and obtain a total of 31 features, $\mathcal{T}_j$, $j = 1, 2, ..., 31$, as discussed in Sect. 4.2.3. We use an error metric $\mathsf{err}_{\mathbf{T}}$ to decide the optimal number of features, $K_{\mathcal{T}}$. The error metric is defined as follows:

$$\mathsf{err}_{\mathbf{T}}(k) = \frac{1}{\mathcal{M}} \sum_{i=1}^{\mathcal{M}} \frac{\|\mathbf{T}_{i,:} - \hat{\mathbf{T}}_{i,:}(k)\|_2}{\|\mathbf{T}_{i,:}\|_2}. \tag{19}$$

It is an averaged relative error between the actual temperature snapshot matrix, $\mathbf{T}_{i,:}$, and its approximation, $\hat{\mathbf{T}}_{i,:}(k)$. Note that we estimate $\hat{\mathbf{T}}_{i,:}(k)$ using the k singular value-singular vector pairs. We calculate the average error with $\mathcal{M}$ = 120 training samples. We plot $\mathsf{err}_{\mathbf{T}}(k)$ versus k in Fig. 5a. It can be seen that the top two features yield an error of less than 5%; therefore, we choose $K_{\mathcal{T}} = 2$.

The surrogate models for the top two features are trained with $\mathcal{M}$=120 samples as described in Algorithm 2.1. The accuracy of the surrogate model is evaluated using the coefficient of determination, $R^2 = 1 - \mathrm{SS}_{\mathrm{res}}/\mathrm{SS}_{\mathrm{tot}}$, where $\mathrm{SS}_{\mathrm{res}}$ is the residual sum of squares and $\mathrm{SS}_{\mathrm{tot}}$ is the total sum of squares. The R^2 score measures the proportion of variance in the model output, and an R^2 value close to one indicates a high accuracy. We use a linear regression model as the form as surrogate model for feature 1 and a parabolic function for feature 2. Both features incorporate only one active variable, achieving R^2 values exceeding 0.9, as seen in Fig. 6.

5.2.2 Residual stress surrogate model

We perform an SVD on $\mathbf{S} \in \mathbb{R}^{120\times 448}$ and obtain a total of 120 features, $\mathcal{S}_j$, $j = 1, 2, ..., 120$, as discussed in Sect. 4.2.4. Similar to the thermal case, we use an error metric $\mathsf{err}_{\mathbf{S}}$ to select the optimal number of features, $K_{\mathcal{S}}$. The error metric is defined as follows:

$$\mathsf{err}_{\mathbf{S}}(k) = \frac{1}{\mathcal{M}} \sum_{i=1}^{\mathcal{M}} \frac{\|\mathbf{S}_{i,:} - \hat{\mathbf{S}}_{i,:}(k)\|_2}{\|\mathbf{S}_{i,:}\|_2}. \tag{20}$$

It is an averaged relative error between the actual temperature snapshot matrix, $\mathbf{S}_{i,:}$, and its approximation, $\hat{\mathbf{S}}_{i,:}(k)$. Similar to the thermal case, we estimate $\hat{\mathbf{S}}_{i,:}$ using the k singular value–singular vector pairs and calculate the average error with $\mathcal{M} = 120$ training samples.

We plot $\mathsf{err}_{\mathbf{S}}$ versus k in Fig. 5b. We observe that $\mathsf{err}_{\mathbf{S}}$ decays slower compared to $\mathsf{err}_{\mathbf{T}}$, which can be attributed

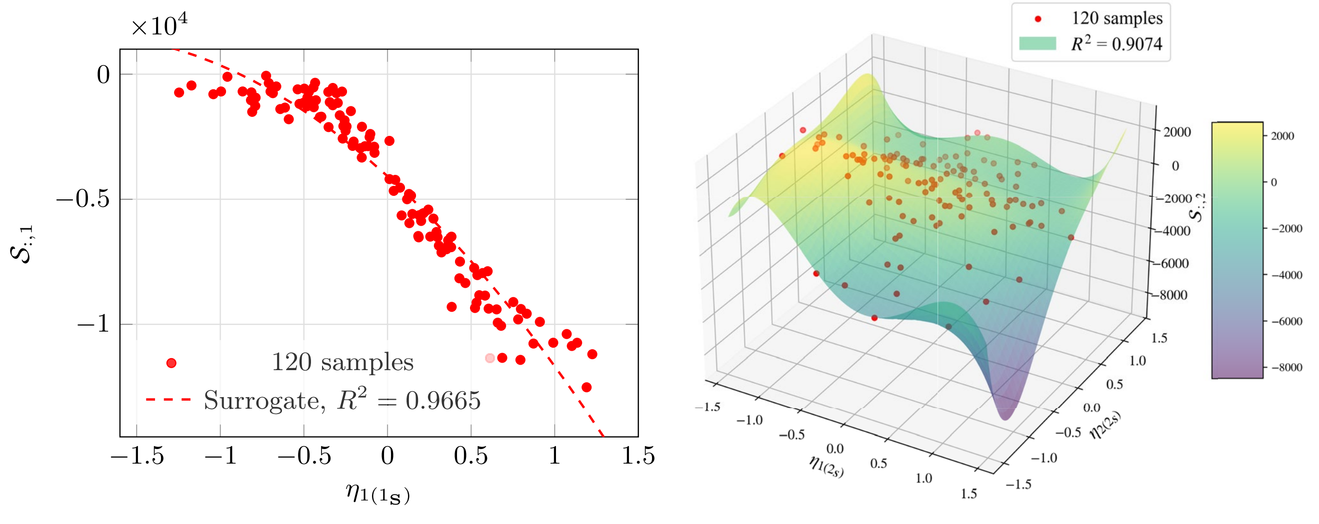

(a) Feature 1. (b) Feature 2.

Fig. 7 Surrogate models for the first two features of the residual stress data

Table 3 Optimization results of different initial designs

Case	Initial Designs			Optimization Results				
	$\mathbf{d}^{\{0\}}$		E [J]	Algorithm	$\mathbf{d}^{*}$		E^{*} [J]	ζ^{*} [MPa]
	v [mm/s]	P [W]			v^{*} [mm/s]	P^{*} [W]		
1	500	160	0.64	SLSQP	465.4	91.0	0.391	717.3
				COBYLA	614.5	115.8	0.377	743.8
2	400	100	0.50	SLSQP	373.0	75.5	0.405	699.1
				COBYLA	417.3	83.0	0.398	709.5
3	400	125	0.625	SLSQP	374.8	75.8	0.404	699.7
				COBYLA	543.9	104.1	0.383	728.8
4	600	100	0.33	SLSQP	539.5	103.4	0.383	728.3
				COBYLA	637.4	119.6	0.375	750.3

All solutions converge to an energy consumption of approximately 0.4 J

to the stress calculation's inherent complexity. The stress is derived from the mechanical finite element model using the thermal model's output, as discussed in Sect. 3.4. The one-way thermal–mechanical coupling introduces additional computational intricacies. To achieve $\mathrm{err}_S < 5\%$, we need $K_S > 5$, i.e., the number of features for surrogate modeling becomes prohibitively large. The later features also prove challenging to model accurately, for example, for feature 6, the coefficient of determination $R^2 = 0.3433$ with a sixth-degree polynomial surface using two active variables. In addition, the value of err_S only decreases from 10.37% to 9.28% when k increases from 5 to 6. Therefore, we choose $K_S = 5$.

We construct surrogate models for the top five features of the residual stress field. We build a parabola surrogate model with one active variable for feature 1 and its R^2 value is greater than 0.96. Feature 2 uses two active variables, its R^2 value is greater than 0.90 with a fifth-degree polynomial surrogate model. We show the surrogate models for these two features in Fig. 7. We list the number of active variables used, polynomial type and R^2 value of the surrogate model for each feature in Table 2.

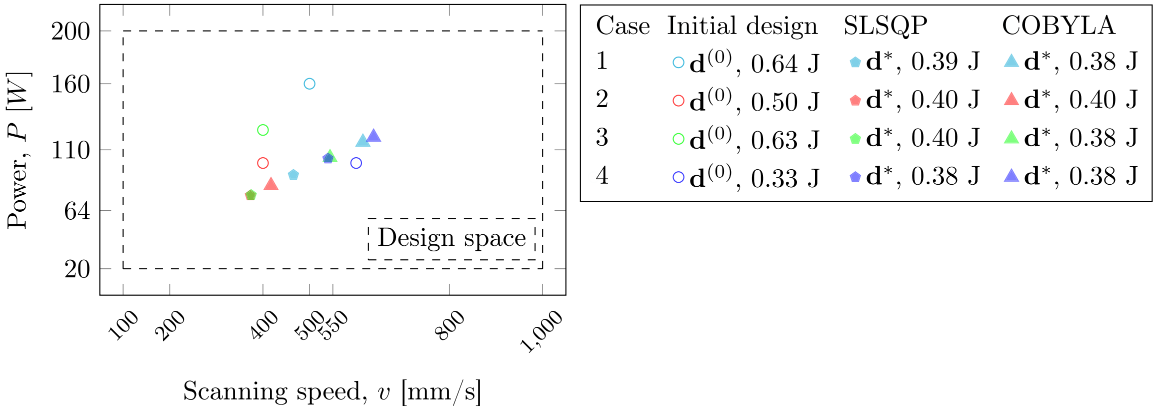

Fig. 8 Comparison of optimization results with different initial designs and optimization solvers. Initial design points (circles) and final optimized solutions from the SLSQP solver (pentagons) and COBYLA solver (triangles) are displayed within the bounded design space (indicated by the dashed box). All optimal $[v, P]$ solutions converge to approximately 0.4 J of consumed energy, independent of the initial design

Table 4 Validation results with the high-fidelity FEM model at two optimal solutions

$\mathbf{d}^{*}$	$\bar{Q}_{0.95}^{\mathrm{FEM}}$	$\bar{Q}_{0.95}^{\mathrm{Surr}}$	$(\bar{Q}_{0.95}^{\mathrm{FEM}} - \bar{Q}_{0.95}^{\mathrm{Surr}})/\bar{Q}_{0.95}^{\mathrm{FEM}}$
[417.3 mm/s, 83.0 W]	768.12 MPa	762.08 MPa	0.79%
[614.5 mm/s, 115.8 W]	790.69 MPa	804.89 MPa	−1.80%

5.3 Optimization results

We perform optimization with multiple initial designs using both SLSQP and COBYLA solvers in SciPy (Virtanen et al. 2020) v1.1.2. We use the default value (1×10^{-6}) as the tolerance precision of the target function in the stopping criterion for the SLSQP solver; for the COBYLA solver, we take the default value (1×10^{-4}) as the lower bound on the size of the trust region. We use $\mathcal{N} = 20{,}000$ samples to estimate expectations in Algorithm 2.2 and set the target reliability level $\alpha_T = 0.95$.

The optimization problem (17) is not globally convex, therefore, both the SLSQP and COBYLA solvers find a local optimum given an initial design. We start the optimization with four different initial designs. For each case, we list the initial design and the corresponding optimization result in Table 3 and plot them in Fig. 8. The consumed energy is calculated using formula $E = P \cdot t = P \cdot l/v$. In Fig. 8, we use the same color to mark each case; the initial design is marked with a circle, the optimal designs obtained by SLSQP and COBYLA solvers are marked with a pentagon and a triangle, respectively (Fig. 8).

The initial designs in case 2 and case 3 have the same scanning speed values but different beam power values. The SLSQP-optimized designs in both cases converge to nearly identical values for both parameters. In contrast, cases 2 and 4, which start with the same beam power but different scanning speeds, yield distinctly different optimal designs. This demonstrates the sensitivity of the optimization process to initial scanning speed values while suggesting robustness with respect to initial beam power selection.

In the optimization problem (17), our primary objective is to minimize energy consumption. The results show decreased energy consumption at the local optima, despite obtaining different optimal configurations for scanning speed and beam power across all cases. The set of process parameters in the initial design of case 4 yields an energy consumption of 0.33 J. Although it is smaller than the optimal result of 0.38 J, with this parameter setting, the maximum temperature in the powder bed in the manufacturing

Table 5 Optimization results comparison between BPOF-constrained formulation and POF-constrained formulation (RBDO) with different initial designs. All optimizations are performed using the SLSQP solver

Case	Initial Designs			Optimization Results				
	$\mathbf{d}^{\{0\}}$		E [J]	Constraint	$\mathbf{d}^*$		E^* [J]	$\bar{Q}_{0.95}$ [MPa]
	v [mm/s]	P [W]			v^* [mm/s]	P^* [W]		$Q_{0.95}$ [MPa]
1	500	160	0.64	BPOF	465.4	91.0	0.391	772.8
				POF	510.7	98.6	0.386	723.5
2	400	100	0.50	BPOF	373.0	75.5	0.405	750.3
				POF	404.8	80.9	0.400	707.0
3	400	125	0.625	BPOF	374.8	75.8	0.404	751.0
				POF	407.6	81.3	0.399	707.5
4	600	100	0.33	BPOF	539.5	103.4	0.383	802.9
				POF	598.1	113.1	0.378	739.7

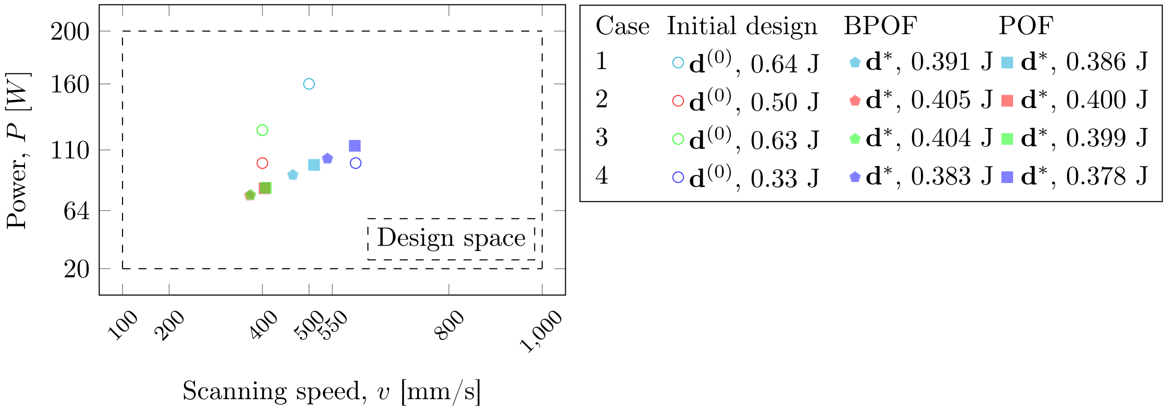

Fig. 9 Comparison of optimization results with different constraint options and initial designs. Initial design points (circles) and final optimized solutions from the BPOF-constrained design (pentagons) and POF-constrained (squares) are displayed within the bounded design space (indicated by the dashed box)

process is $T_{\max} = 1{,}556°\mathrm{C} < T_{\mathrm{liq}} = 1{,}650°\mathrm{C}$, which does not satisfy the temperature constraint in (17) and indicates no powder melting. The $T_{\max}$ values corresponding to the optimal parameters obtained with SLSQP and COBYLA solvers in case 4 are both 1,655°C, which satisfies the temperature constraint. For all other cases, we see a reduction in the consumed energy from the initial designs to the optimal results. While different initial designs yield varying optimal results, all solutions converge to an energy consumption of approximately 0.4 J. This consistency across different initial designs shows the robustness of our optimization approach while providing valuable guidance for selecting appropriate scanning speed and beam power.

5.4 Validation

We validate the optimal designs via their corresponding risk-based constraints on the maximum residual stress $\sigma_{\max}$. Specifically, we examine the 0.95-superquantiles of $\sigma_{\max}$ corresponding to optimal designs. The optimal auxiliary variable ζ^* can be viewed as the 0.95-quantile of $\sigma_{\max}$ related to its corresponding optimal parameter vector $\mathbf{d}^*$, as discussed in Sect. 4.1. We then can use $\mathbf{d}^*$, ζ^*, and samples of the random variable Z to estimate the 0.95-superquantile with (9).

Due to computational limitations, we validate two optimization results listed in Table 3. For each optimum, we conduct 50 additional FEM simulations and compare the 0.95-superquantile from these simulations, $\bar{Q}_{0.95}^{\mathsf{FEM}}$, with the 0.95-superquantile estimated from 20,000 surrogate model evaluations, $\bar{Q}_{0.95}^{\mathsf{Surr}}$. We generate random samples of Z to create realizations of the vector $[\mathbf{d}^{*\top}, Z^\top; \boldsymbol{\theta}^\top]^\top$, which serve as inputs for the FEM simulations and the surrogate models $\hat{G}_{S_{:,j}}(\boldsymbol{\eta}_{(j_S)})$ for $j_{\mathsf{S}} = 1, 2, 3, 4, 5$. For FEM simulations, we obtain the residual stress field directly from the output, while for surrogate evaluations, we estimate it using (18). For each optimum $\mathbf{d}^*$, with the samples of $\sigma_{\max}$ and the optimal auxiliary variable ζ^* corresponding to $\mathbf{d}^*$, we calculate $\bar{Q}_{0.95}^{\mathsf{FEM}}$ and $\bar{Q}_{0.95}^{\mathsf{Surr}}$ using (9) and present the results in Table 4. Although both validation sets only use 50 Monte Carlo samples for FEM simulations, which introduces sampling error, both superquantiles $\bar{Q}_{0.95}^{\mathsf{FEM}}$ and $\bar{Q}_{0.95}^{\mathsf{Surr}}$ closely match each other for both optimal results. This suggests that our approach maintains accuracy despite the limited sampling and confirms that integrating surrogate models into the optimization process produces reliable outcomes.

5.5 Comparison with reliability-based design optimization

We compare the optimal designs from both the BPOF-constrained design formulation (17) and a more traditional reliability-based design optimization (RBDO) formulation that uses a probability of failure (POF), e.g.,

$$\begin{aligned} \min_{\substack{P_L \le P \le P_U,\\ v_L \le v \le v_U}} \quad & P \cdot \frac{l}{v} \\ \text{subject to} \quad & p(\sigma_{\max}(\mathbf{d}, Z; \boldsymbol{\theta})) \le 1 - \alpha_T, \\ & T_{\mathrm{liq}} < T_{\max}(\mathbf{d}, Z; \boldsymbol{\theta}) < 1.1 \times T_{\mathrm{liq}}. \end{aligned} \tag{21}$$

For the RBDO problem (21), we use the same target reliability level $\alpha_T = 0.95$ as we use for the BPOF-constrained design formulation (17). We solve it with the same initial designs, and by the SLSQP solver as discussed above. We use 20, 000 samples to estimate Q_α per Algorithm 1 to obtain the failure probability p_τ in (21) according to (8). We compare the results in Table 5 and plot them in Fig. 9. Using the same approach for calculating $\bar{Q}_{0.95}^{\mathsf{Surr}}$ in validation, here, we generate random samples of Z to create realizations of the vector $[\mathbf{d}^{*\top}, Z^\top; \boldsymbol{\theta}^\top]^\top$ that serve as inputs to the surrogate models $\hat{G}_{S_{:,j}}(\boldsymbol{\eta}_{(j_S)})$ for $j_{\mathsf{S}} = 1, 2, 3, 4, 5$. We use the 20,000 surrogate model predictions to estimate the 0.95-quantile $Q_{0.95}$ and 0.95-superquantile $\bar{Q}_{0.95}$ per Algorithm 1 and list them in Table 5 (Fig. 9).

The BPOF-constrained design optimization offers a key advantage in its conservative approach. It considers the tails of the distribution of the quantity of interest by accounting for the magnitude of the failure. This data-informed conservativeness is more resilient to severe and catastrophic failures. A comparison of the consumed energy values and a comparison of the 0.95-superquantile against the 0.95-quantile reveal slightly higher values for the BPOF-constrained designs in all four cases, which indicates greater conservativeness at the same target reliability level. This conservativeness stems from the BPOF formulation, which accounts for both the magnitude and frequency of failures. In contrast, POF-constrained optimization (RBDO) typically relies on manually applied safety factors or stricter reliability levels to enhance conservativeness. Such safety factors, however, can result in overly conservative designs without considering the distribution of the limit state function, thus lacking sufficient information for informed decision-making. Conversely, BPOF-constrained designs incorporate more comprehensive data on the magnitude of failures, embedding conservativeness through a deeper understanding of the underlying limit state function. The data-informed conservativeness of BPOF-constrained designs, driven by the distribution of performance measures rather than arbitrary safety factors or stricter reliability levels used in RBDO, yields more resilient and desirable outcomes.

6 Conclusion and future work

We formulated and solved a buffered probability of failure-constrained design optimization under uncertainty problem for powder bed fusion metal additive manufacturing with the goal to minimize energy consumption while enhancing manufacturing quality. We simulated the manufacturing process to capture the thermal and mechanical behaviors of the manufactured part by conducting high-fidelity finite element analyses. Based on the simulation data, we developed efficient surrogate models using singular value decomposition and active subspace discovery for temporal and spatial quantities of interest, namely the temperature history and residual stress field, to reduce computational costs while maintaining prediction accuracy. Finally, we validated the optimization results through additional finite element simulations. The validation results confirm decreased energy consumption and reduced build failures.

In the future, this work can be refined with an improved two-way-coupled thermal-mechanical finite element model and a finer mesh. We furthermore plan to extend the PBOF-constrained optimization to more complex geometries by incorporating the printing path into the optimization formulation.

Acknowledgements Funding information: Y. Guo and B. Kramer were financially supported by the Air Force Office of Scientific Research (PM Fahroo) under award number FA9550-24-1-0237 and the Defense Advanced Research Projects Agency (DARPA) Cooperative Agreement No. HR0011-25-2-0009, "Predictive Real-time Intelligence for Metallic Endurance (PRIME)."

Author contributions Yulin Guo contributed toward conceptualization, methodology, data curation, software, formal analysis, investigation, software, visualization, and writing—original draft; Boris Kramer contributed toward conceptualization, formal analysis, writing—review and editing, funding acquisition, project administration, and supervision.

Data availability Input files for Abaqus simulations and the complete data sets used to generate the results are available to download from the Github repository: https://github.com/yulin-g/BPOF-optimization-AM.

Declarations

Conflict of interest Boris Kramer reports a relationship with ASML Holding US that includes consulting or advisory. Yulin Guo declares that he has no known competing financial interests or personal relationships that could have appeared to influence the work reported in this paper.

Replication of results The results presented in this manuscript can be fully replicated using the provided material in the Github repository.

References

Bartlett JL, Li X (2019) An overview of residual stresses in metal powder bed fusion. Addit Manuf 27:131–149

Bhardwaj T, Shukla M, Paul C, Bindra K (2019) Direct energy deposition-laser additive manufacturing of titanium-molybdenum alloy: parametric studies, microstructure and mechanical properties. J Alloy Compd 787:1238–1248

Cansizoglu O, Harrysson OL, West HA, Cormier DR, Mahale T (2008) Applications of structural optimization in direct metal fabrication. Rapid Prototyp J 14(2):114–122

Cao L, Li J, Hu J, Liu H, Wu Y, Zhou Q (2021) Optimization of surface roughness and dimensional accuracy in LPBF additive manufacturing. Opt Laser Technol 142:107246

Chastand V, Quaegebeur P, Maia W, Charkaluk E (2018) Comparative study of fatigue properties of Ti-6Al-4V specimens built by electron beam melting (EBM) and selective laser melting (SLM). Mater Charact 143:76–81

Chaudhuri A, Kramer B, Norton M, Royset JO, Willcox K (2022) Certifiable risk-based engineering design optimization. AIAA J 60(2):551–565

Chia HY, Wu J, Wang X, Yan W (2022) Process parameter optimization of metal additive manufacturing: a review and outlook. J Mater Inf 2:4

Constantine PG (2015) Active subspaces. Society for Industrial and Applied Mathematics, Philadelphia

Corbin DJ, Nassar AR, Reutzel EW, Beese AM, Michaleris P (2018) Effect of substrate thickness and preheating on the distortion of laser deposited Ti-6Al-4V. J Manuf Sci Eng 140(6):061009

Debroy T, Zhang W, Turner J, Babu SS (2017) Building digital twins of 3D printing machines. Scripta Mater 135:119–124

Elsayed M, Ghazy M, Youssef Y, Essa K (2018) Optimization of SLM process parameters for Ti6Al4V medical implants. Rapid Prototyp J 25(3):433–447

Everton SK, Hirsch M, Stravroulakis P, Leach RK, Clare AT (2016) Review of in-situ process monitoring and in-situ metrology for metal additive manufacturing. Mater Design 95:431–445

Fu C, Guo Y (2014) 3-dimensional finite element modeling of selective laser melting Ti-6Al-4V alloy. In: Proceedings of the 2014 international solid freeform fabrication symposium, University of Texas at Austin, 1129–1144

Gaikwad A, Giera B, Guss GM, Forien J-B, Matthews MJ, Rao P (2020) Heterogeneous sensing and scientific machine learning for quality assurance in laser powder bed fusion-a single-track study. Addit Manuf 36:101659

Galarraga H, Lados DA, Dehoff RR, Kirka MM, Nandwana P (2016) Effects of the microstructure and porosity on properties of Ti-6Al-4V ELI alloy fabricated by electron beam melting (EBM). Addit Manuf 10:47–57

Gibson I, Rosen DW, Stucker B, Khorasani M, Rosen D, Stucker B, Khorasani M (2021) Additive manufacturing technologies, Springer

Gong H, Rafi K, Gu H, Starr T, Stucker B (2014) Analysis of defect generation in Ti-6Al-4V parts made using powder bed fusion additive manufacturing processes. Addit Manuf 1:87–98

Gong H, Rafi K, Gu H, Ram GJ, Starr T, Stucker B (2015) Influence of defects on mechanical properties of Ti-6Al-4V components produced by selective laser melting and electron beam melting. Mater Design 86:545–554

International Organization for Standardization, American Society for Testing and Materials (2021) *ISO/ASTM52900 Additive manufacturing - General principles - Fundamentals and vocabulary*. Version F3177-21

Kalentics N, Boillat E, Peyre P, Ćirić-Kostić S, Bogojević N, Logé RE (2017) Tailoring residual stress profile of selective laser melted parts by laser shock peening. Addit Manuf 16:90–97

Karlsson J, Snis A, Engqvist H, Lausmaa J (2013) Characterization and comparison of materials produced by electron beam melting (EBM) of two different Ti-6Al-4V powder fractions. J Mater Process Technol 213(12):2109–2118

Konda Gokuldoss P, Kolla S, Eckert J (2017) Additive manufacturing processes: selective laser melting, electron beam melting and binder jetting-selection guidelines. Materials 10(6):672

Lee D, Rahman S (2021) Robust design optimization under dependent random variables by a generalized polynomial chaos expansion. Struct Multidisc Optim 63(5):2425–2457

Li C, Liu Z, Fang X, Guo Y (2018) Residual stress in metal additive manufacturing. Procedia CIRP 71:348–353

Lu Y, Wu S, Gan Y, Huang T, Yang C, Junjie L, Lin J (2015) Study on the microstructure, mechanical property and residual stress of SLM Inconel-718 alloy manufactured by differing island scanning strategy. Opt Laser Technol 75:197–206

Lu W, Zhai W, Wang J, Liu X, Zhou L, Ibrahim AMM, Li X, Lin D, Wang YM (2021) Additive manufacturing of isotropic-grained, high-strength and high-ductility copper alloys. Addit Manuf 38:101751

Megahed M, Mindt H-W, N'Dri N, Duan H, Desmaison O (2016) Metal additive-manufacturing process and residual stress modeling. Integrat Mater Manuf Innov 5(1):61–93

Meng L, Zhang J (2020) Process design of laser powder bed fusion of stainless steel using a gaussian process-based machine learning model. JOM 72(1):420–428

Murr LE (2018) Additive manufacturing of biomedical devices: an overview. Mater Technol 33(1):57–70

Mur FG, Rodríguez D, Planell J (1996) Influence of tempering temperature and time on the α'-Ti-6Al-4V martensite. J Alloy Compd 234(2):287–289

Oyesola M, Mpofu K, Mathe N, Fatoba S, Hoosain S, Daniyan I (2021) Optimization of selective laser melting process parameters for surface quality performance of the fabricated Ti6Al4V. Int J Adv Manuf Technol 114:1585–1599

Rockafellar RT, Uryasev S (2002) Conditional value-at-risk for general loss distributions. J Bank Finance 26(7):1443–1471

Rockafellar RT, Royset JO (2010) On buffered failure probability in design and optimization of structures. Reliab Eng Syst Saf 95(5):499–510

Seoane-Viaño I, Januskaite P, Alvarez-Lorenzo C, Basit AW, Goyanes A (2021) Semi-solid extrusion 3D printing in drug delivery and biomedicine: personalised solutions for healthcare challenges. J Control Release 332:367–389

Shapiro AA, Borgonia J, Chen Q, Dillon R, McEnerney B, Polit-Casillas R, Soloway L (2016) Additive manufacturing for aerospace flight applications. J Spacecraft Rockets, 952–959

Shi X, Ma S, Liu C, Wu Q (2017) Parameter optimization for Ti-47Al-2Cr-2Nb in selective laser melting based on geometric characteristics of single scan tracks. Opt Laser Technol 90:71–79

Shiomi M, Osakada K, Nakamura K, Yamashita T, Abe F (2004) Residual stress within metallic model made by selective laser melting process. CIRP Ann 53(1):195–198

Spears TG, Gold SA (2016) In-process sensing in selective laser melting (SLM) additive manufacturing. Integrat Mater Manuf Innov 5(1):16–40

Sun J, Yang Y, Wang D (2013) Parametric optimization of selective laser melting for forming Ti6Al4V samples by Taguchi method. Opt Laser Technol 49:118–124

Vasco JC (2021) Additive manufacturing for the automotive industry. In: Additive manufacturing. Elsevier, 505–530

Vastola G, Zhang G, Pei Q, Zhang Y-W (2016) Controlling of residual stress in additive manufacturing of Ti6Al4V by finite element modeling. Addit Manuf 12:231–239

Vilaro T, Colin C, Bartout J-D (2011) As-fabricated and heat-treated microstructures of the Ti-6Al-4V alloy processed by selective laser melting. Metall Mater Trans A 42(10):3190–3199

Virtanen P, Gommers R, Oliphant TE, Haberland M, Reddy T, Cournapeau D, Burovski E, Peterson P, Weckesser W, Bright J, van der Walt SJ, Brett M, Wilson J, Millman KJ, Mayorov N, Nelson ARJ, Jones E, Kern R, Larson E, Carey CJ, Polat İ, Feng Y, Moore EW, VanderPlas J, Laxalde D, Perktold J, Cimrman R, Henriksen I, Quintero EA, Harris CR, Archibald AM, Ribeiro AH, Pedregosa F, van Mulbregt P (2020) SciPy 1.0 Contributors. SciPy 1.0: Fundamental algorithms for scientific computing in python. Nat Methods 17:261–272

Vohra M, Nath P, Mahadevan S, Tina Lee Y-T (2020) Fast surrogate modeling using dimensionality reduction in model inputs and field output: application to additive manufacturing. Reliab Eng Syst Saf 201:106986

Wang Z, Liu P, Xiao Y, Cui X, Hu Z, Chen L (2019) A data-driven approach for process optimization of metallic additive manufacturing under uncertainty. J Manuf Sci Eng 141(8):081004

Wang H, Li B, Lei L, Xuan F (2024) Uncertainty-aware fatigue-life prediction of additively manufactured Hastelloy X superalloy using a physics-informed probabilistic neural network. Reliab Eng Syst Saf 243:109852

Wei D, Koizumi Y, Chiba A, Ueki K, Ueda K, Narushima T, Tsutsumi Y, Hanawa T (2018) Heterogeneous microstructures and corrosion resistance of biomedical Co-Cr-Mo alloy fabricated by electron beam melting (EBM). Addit Manuf 24:103–114

Welsch G, Boyer R, Collings E (1993) Materials properties handbook: titanium alloys. ASM international

Wu AS, Brown DW, Kumar M, Gallegos GF, King WE (2014) An experimental investigation into additive manufacturing-induced residual stresses in 316L stainless steel. Metall Mater Trans A 45:6260–6270

Yadroitsev I, Krakhmalev P, Yadroitsava I, Johansson S, Smurov I (2013) Energy input effect on morphology and microstructure of selective laser melting single track from metallic powder. J Mater Process Technol 213(4):606–613

Yan W, Ge W, Qian Y, Lin S, Zhou B, Liu WK, Lin F, Wagner GJ (2017) Multi-physics modeling of single/multiple-track defect mechanisms in electron beam selective melting. Acta Mater 134:324–333

Zhao X, Promoppatum P, Yao S-C (2015) Numerical modeling of non-linear thermal stress in direct metal laser sintering process of titanium alloy products. In: Proceedings of the first thermal and fluids engineering summer conference, 9–12

Zinoviev A, Zinovieva O, Ploshikhin V, Romanova V, Balokhonov R (2016) Evolution of grain structure during laser additive manufacturing simulation by a cellular automata method. Mater Design 106:321–329

Zou T, Mahadevan S (2006) A direct decoupling approach for efficient reliability-based design optimization. Struct Multidisc Optim 31:190–200